

JGR Solid Earth

RESEARCH ARTICLE

10.1029/2023JB028062

Key Points:

- A high-resolution broadband Pn attenuation model is obtained beneath the Iranian Plateau
- Weak Pn attenuation delineates the underthrusting front of the Arabian Plate and reveals the segmented plate up-bending
- Post-collision magmatism is likely related to the detachment-related mantle upwelling characterized by strong Pn attenuation

Supporting Information:

Supporting Information may be found in the online version of this article.

Correspondence to:

L.-F. Zhao,
zhaolf@mail.iggcas.ac.cn

Citation:

Yang, G., Chen, L., Zhao, L.-F., Xie, X.-B., & Yao, Z.-X. (2023). Segmented up-bending of the Arabian continental plate revealed by Pn attenuation tomography. *Journal of Geophysical Research: Solid Earth*, 128, e2023JB028062. <https://doi.org/10.1029/2023JB028062>

Received 12 OCT 2023

Accepted 12 DEC 2023

Author Contributions:

Conceptualization: Geng Yang, Ling Chen, Lian-Feng Zhao, Xiao-Bi Xie
Data curation: Ling Chen, Lian-Feng Zhao
Formal analysis: Geng Yang, Ling Chen
Funding acquisition: Ling Chen, Lian-Feng Zhao, Zhen-Xing Yao
Investigation: Geng Yang
Methodology: Geng Yang, Lian-Feng Zhao, Xiao-Bi Xie
Project Administration: Ling Chen, Lian-Feng Zhao, Zhen-Xing Yao
Resources: Ling Chen, Lian-Feng Zhao
Software: Geng Yang, Lian-Feng Zhao
Supervision: Ling Chen, Lian-Feng Zhao, Xiao-Bi Xie, Zhen-Xing Yao
Validation: Geng Yang
Visualization: Geng Yang
Writing – original draft: Geng Yang

Segmented Up-Bending of the Arabian Continental Plate Revealed by Pn Attenuation Tomography

Geng Yang^{1,2} , Ling Chen^{2,3}, Lian-Feng Zhao^{1,4} , Xiao-Bi Xie⁵, and Zhen-Xing Yao¹ 

¹Key Laboratory of Earth and Planetary Physics, Institute of Geology and Geophysics, Chinese Academy of Sciences, Beijing, China, ²College of Earth and Planetary Sciences, University of Chinese Academy of Sciences, Beijing, China, ³State Key Laboratory of Lithosphere Evolution, Institute of Geology and Geophysics, Chinese Academy of Sciences, Beijing, China, ⁴Heilongjiang Mohe Observatory of Geophysics, Institute of Geology and Geophysics, Chinese Academy of Sciences, Beijing, China, ⁵Institute of Geophysics and Planetary Physics, University of California at Santa Cruz, Santa Cruz, CA, USA

Abstract The Zagros orogen in the Iranian Plateau serves as a natural laboratory for studying the tectonic evolution of the transition from oceanic subduction to continental collision. Various observations from both geology and geophysics show that deep oceanic slabs may have detached one after another from the Arabian continental margin, forming a complex plate front beneath the Zagros orogen. However, where slab detachment occurred and how slab detachment affects shallower continental underthrusting remain poorly understood. The mechanism behind the complex post-collision magmatism remains elusive. While the uppermost mantle is often considered the heart of the mantle lid, its rheological variations can provide insights into the underlying thermal structure. Here, we construct a high-resolution Pn-wave attenuation model for the uppermost mantle beneath the Iranian Plateau and surrounding areas using a newly compiled data set and constrain the lithospheric structure by combining the Lg-wave attenuation within the crust. Weak Pn-wave attenuation outlines the boundary of the Arabian Plate near the Moho discontinuity, extending further in the direction of underthrusting in the northwestern and southeastern regions. This is likely due to the up-bending and underplating of the Arabian lithosphere following the cessation of slab pull. The overlying crusts in northwestern and southeastern Zagros thickened under the compressive force from plate underplating. The correlations among the surface Miocene-Quaternary volcanism, strong Lg attenuation in the crust and strong Pn attenuation in the uppermost mantle suggest that asthenospheric materials escaped from slab windows and further intruded into the upper mantle and crust to feed the post-collision volcanoes.

Plain Language Summary Various geological and geophysical observations show that deep oceanic slabs may have detached one after another from the Arabian continental margin, forming a complex plate front beneath the Iranian Plateau. However, the processes of continental underthrusting and collision remain poorly understood. The formation mechanism of the complex magmatism in the Iranian Plateau is also unclear. The uppermost mantle, often considered the core of the mantle lid, exhibits rheological variations that can provide insights into the underlying thermal structure. In this study, we conducted high-resolution Pn-wave attenuation tomography for the uppermost mantle beneath the Iranian Plateau, using 23,251 vertical-component waveforms recorded at 291 previous stations and 197 new temporary stations. The resulting images show that the cold Arabian plate is characterized by weak Pn attenuation beneath the Zagros orogen and the strong attenuation anomalies are related to younger magmatism. Combined with previous geological and geochemical observations, our results suggest a successive evolution process under the Iranian Plateau. The ancient Neotethys oceanic plate partially detached from the Arabian continental margin. After the slab break-off at depth, the Arabian continental plate rose back and flattened below the overriding plate. Meanwhile, the detachment-related asthenosphere upwelling fed the younger volcanism at the surface.

1. Introduction

Plate convergence processes determine the formation and evolution of plateaus, such as the Iranian, Anatolian, and Tibetan plateaus. During the transition from oceanic subduction to continental collision, a descending slab may experience an increase in tensile stress between its deep and shallow portions and further break off, a phenomenon attributed to the strong buoyancy generated by continental crust subduction at relatively shallow depths (Davies & Blanckenburg, 1995; Kufner et al., 2021). After slab detachment, the subducted continental lithosphere loses the drag force of the deep slab and hence possibly up-bends toward the overriding plate (Li

Writing – review & editing: Geng Yang, Ling Chen, Lian-Feng Zhao, Xiao-Bi Xie

et al., 2013; van Hunen & Allen, 2011). In this situation, asthenospheric flow is likely triggered around the broken edges of the plate (e.g., Guivel et al., 2006; Kundu & Gahalaut, 2011). Although numerical modeling can simulate the processes of continental underthrusting and collision (Gao et al., 2023; Li et al., 2013; Magni et al., 2017; van Hunen & Allen, 2011), unraveling the intricate workings of its geodynamics necessitates additional insights gleaned from a comprehensive suite of geological and geophysical observations, including seismic velocity and attenuation tomography (Stern et al., 2021).

The Zagros orogen, a fold-thrust belt in the Iranian Plateau, lies within the Alpine-Zagros-Himalayan convergent zone, a vast region of continental collision that emerged following the closure of the Neotethys Ocean and the collision of the Arabian and Eurasian plates (Figure 1) (e.g., Chemenda et al., 2000; Li et al., 2013; Mousavi, 2017a; Stern et al., 2021). Seismic tomography revealed that the Neotethyan plate subducted northward and that the deep oceanic slab partially detached from the Arabian continental margin (e.g., Alinaghi et al., 2007; Hafkenscheid et al., 2006; Mahmoodabadi et al., 2019; Manaman & Shomali, 2010; Rahmani et al., 2019; Shomali et al., 2011). However, the inconsistent imaging results led to controversy over the detachment locations. The deep oceanic slab may have detached under the northwestern and southeastern Zagros orogen, avoiding the central Zagros (e.g., Agard et al., 2011; Alinaghi et al., 2007; Hafkenscheid et al., 2006; Rahmani et al., 2019; Veisi et al., 2021). Otherwise, an updated velocity model for the Iranian Plateau observed similar discontinuous high-velocity anomalies under the central Zagros (Mahmoodabadi et al., 2019). Although the surface topographic relief is not sensitive to deep plate kinematic processes, shallow Arabian lithosphere tectonics exhibit a strong reaction to slab detachment at depth, manifesting as plate up-bending and underplating (Li et al., 2013; van Hunen & Allen, 2011). Therefore, investigating the detailed structure of the upper mantle is an effective way to understand the entire underthrusting and collision processes.

Both plate subduction and collision led to active magmatism and formed the Urumieh-Dokhtar magmatic arc (UDMA) along the underthrusting front of the Arabian Plate (Verdel et al., 2011). The UDMA extends from the Talesh Caucasus and Alborz Mountains in the northwest to the Makran subduction region in the southeast. Zircon U–Pb age measurements show that the Urumieh-Dokhtar magmatism was most active during the Eocene and Oligocene (55–25 Ma) (Chiu et al., 2013 and references therein) and was controlled by Neotethyan oceanic subduction (e.g., Asadi et al., 2014; Babazadeh et al., 2017). Oceanic subduction ceased due to the continental collision between the Arabian continental margin and the Iranian Plateau, yet volcanism persisted in the northwestern and southeastern segments of the Urumieh-Dokhtar Magmatic Arc (UDMA) into the Miocene-Quaternary period (Chiu et al., 2013). To understand the post-collisional magmatism in the UDMA, several models have been proposed but are controversial, including slab rollback (e.g., Babazadeh et al., 2017), slab break-off (e.g., Ghalamghash et al., 2016; Jahangiri, 2007; Omrani et al., 2008), changes in subduction angle (Shahabpour, 2007), and crustal thickening caused by oblique and diachronous collision (Chiu et al., 2013). Investigating the intricate details of lithospheric thermal structure and establishing connections between deep-seated dynamic processes and surface volcanism is critical for comprehending the evolutionary trajectory of magmatism.

Compared with seismic velocity, seismic attenuation is more sensitive to temperature, partial melting, and fluid (e.g., Artemieva et al., 2004; Boyd et al., 2004; He et al., 2021; Zhu et al., 2013). In this study, we construct a Pn-wave attenuation model in and around the Iranian Plateau to detect the boundary of the Arabian underthrusting front and the potential magma sources in the uppermost mantle. The layered results, including the subcrustal lithospheric thermal structure obtained in this study, crustal thermal anomalies from strong Lg attenuation (G. Yang et al., 2023), and surface volcanic rocks, suggest a successive process from deep geodynamics, including slab break-off, plate up-bending and mantle upwelling, to crustal heat storage and transmission as well as volcanic eruption near the Arabian underthrusting front.

2. Data and Methods

2.1. Regional Data Set

In the Iranian Plateau, the seismicity is more concentrated along the active fold-thrust mountain belts compared to the stable block at the center (Robert Engdahl et al., 2006). The ISC-EHB catalog and previous relocation results showed that most earthquakes occurred in the upper crust (e.g., Nissen et al., 2011, 2019; Robert Engdahl et al., 2006). In this study, a total of 23,251 vertical-component waveforms were collected from 594 crustal earthquakes recorded at 488 broadband stations in and around the Iranian Plateau, where 291 stations belong to

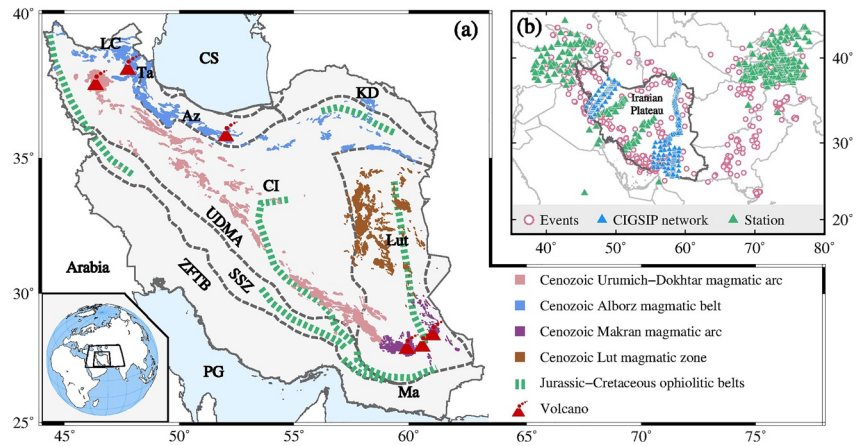


Figure 1. Maps showing the major geological blocks and magmatic belts in the Iranian Plateau (a) and the locations of stations and earthquakes (b). The green stations were collected from the Incorporated Research Institutions for Seismology Data Management Center, the German Research Centre for Geoscience, the International Seismological Centre, and the International Federation of Digital Seismograph Networks. The CIGSIP stations are highlighted in blue. Az: Alborz Mountains; CIGSIP: The China-Iran Geological and Geophysical Survey in the Iranian Plateau during 2013–2018; CI: Central Iranian Basins; CS: Caspian Sea; KD: Kopet-Dogh Mountains; LC: Lesser Caucasus Mountains; Lut: Lut Blocks; Ma: Makran region; OS: Oman Sea; PG: Persian Gulf; SSZ: Sanandaj-Sirjan Zone; Ta: Talesh Mountains; UDMA: Urumieh-Dokhtar magmatic arc; and ZFTB: Zagros Fold-Thrust Belt.

regional networks (see Data Availability Statement), and 197 new stations that belong to three temporary seismic networks in western and eastern Iran established by the “China-Iran Geological and Geophysical Survey in the Iranian Plateau (CIGSIP)” project during 2013–2018 (Gao et al., 2022; Sadeghi-Bagherabadi et al., 2018; Wang et al., 2022; Wu et al., 2021). Earthquakes that occurred above the Moho (Laske et al., 2013) with known focal mechanisms were selected from the Harvard Centroid Moment Tensor catalog (Ekstrom et al., 2012) to facilitate the calculation of the radiation patterns of Pn-waves. The earthquake sizes were confined within a magnitude range of $4.3 \leq m_b \leq 6.5$. Figure S1 in Supporting Information S1 illustrates 72 waveforms from the three temporary CIGSIP networks, bandpass filtered between 0.5 and 8.0 Hz. The Pn signals with different propagation paths were clearly recorded. Detailed station and earthquake information is listed in Tables S1 and S2 in Supporting Information S2.

2.2. Pn-Wave Spectral Amplitude

The Pn amplitude measurement was conducted following the processing procedure from Zhao et al. (2015). As the first arrival phase for regional distances between 200 and 2,000 km, the Pn waveform was sampled in a 0.7 km/s-long group velocity window around the IASP91 first arrival, and the noise was extracted before the P arrival within a window with a time length equal to that of the Pn waveform; both the Pn and noise spectra and SNRs were obtained using the fast Fourier transformation; the Pn data were selected based on an SNR threshold of 2.0, and the Pn signal amplitudes were obtained after denoising (Figure 2).

2.3. Pn-Wave Geometric Spreading

The theoretical spectral amplitude of the Pn-wave can be expressed as (Sereno et al., 1988; J. K. Xie & Patton, 1999)

$$A(f) = S(f) \cdot G(\Delta, f) \cdot \Gamma(\Delta, f) \cdot P(f) \cdot r(f), \quad (1)$$

where $A(f)$ is the Pn amplitude at frequency f , $S(f)$ is the source spectrum, $G(\Delta, f)$ is the geometric spreading factor relative to epicentral distance Δ and frequency f , $\Gamma(\Delta, f)$ is the attenuation term, $P(f)$ is the site response, and $r(f)$ is the random effect. The attenuation term $\Gamma(\Delta, f)$ can be further expressed as

$$\Gamma(\Delta, f) = \exp \left[-\frac{\pi f}{V} B(\Delta, f) \right], \quad (2)$$

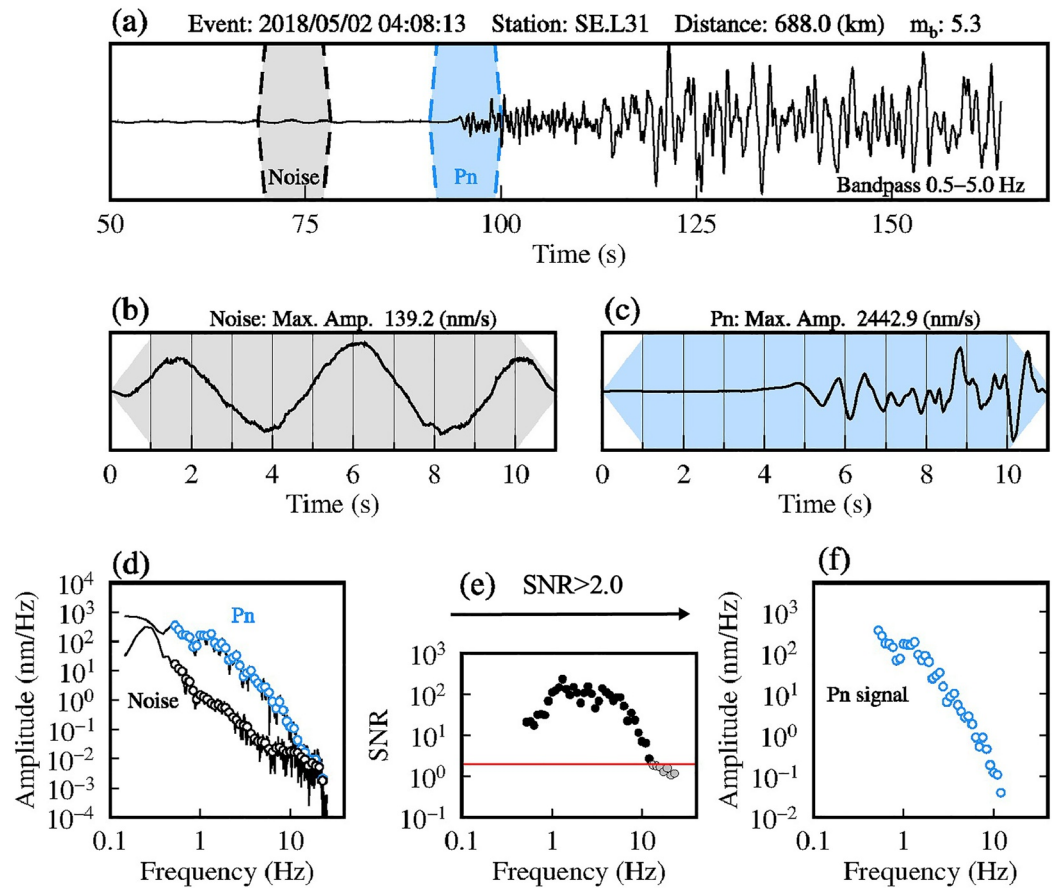


Figure 2. An example of the Pn spectral amplitude measurement. (a) Vertical-component seismograms from the 02 May 2018 earthquake recorded at station SE.L31, where the noise (gray) and Pn signals (blue) were sampled within two equal-time length windows. (b, c) Enlarged waveforms of the noise and Pn signal. (d) Pn and noise spectra. (e) SNR for data selection, where the data with SNR < 2.0 were removed. (f) Denoised Pn spectra.

where V is the velocity of the Pn-wave and $B(\Delta, f) = \int_{\text{ray}} \frac{ds}{Q(f)}$ is the integral of the attenuation over the great circle path (Zhao et al., 2015).

To obtain the attenuation term accurately, it is necessary to reasonably correct the influence of the geometric spreading of the Pn-wave. Numerical modeling suggests that the geometric spreading factor $G(\Delta, f)$ can be expressed in logarithmic-quadratic form (X. N. Yang, 2011; X. Yang et al., 2007):

$$G(\Delta, f) = 10^{\xi_3(f)} \Delta^{\xi_1(f)} \log_{10} \Delta^{-\xi_2(f)}, \quad (3)$$

where $\xi_n(f)$ is related to the logarithm of the frequency,

$$\xi_n(f) = \xi_{n1} \log_{10}^2(f) + \xi_{n2} \log_{10}(f) + \xi_{n3}. \quad (4)$$

The parameters ξ_{ij} could be finely adjusted with $\pm 10\%$ perturbations according to the actual Pn amplitude data (G. Yang et al., 2022; Zhao et al., 2015). Based on Equation 1, the Pn-wave amplitude spectrum was obtained by fitting the geometric spreading and the regional apparent Q_{Pn} in the entire study area and the source functions of the 594 earthquakes (Figure 3). Note that the best-fitting model could reasonably explain the actual Pn amplitude data (Figure 3a). The resulting geometric spreading functions between 0.5 and 20.0 Hz exhibited similar overall shapes that first decreased and then increased with an increasing epicentral distance (Figure 3b). The best-fit apparent attenuation parameters of Q_0 and η were 251 and 0.65, respectively, and yielded $Q_{\text{Pn}} = 251f^{0.65}$ (Figure 3c), where Q_0 was the Q value at 1 Hz, and η was the frequency-dependent coefficient. The seismic moment and corner frequency for each event were further inverted based on the resulting source term (Figure 3d).

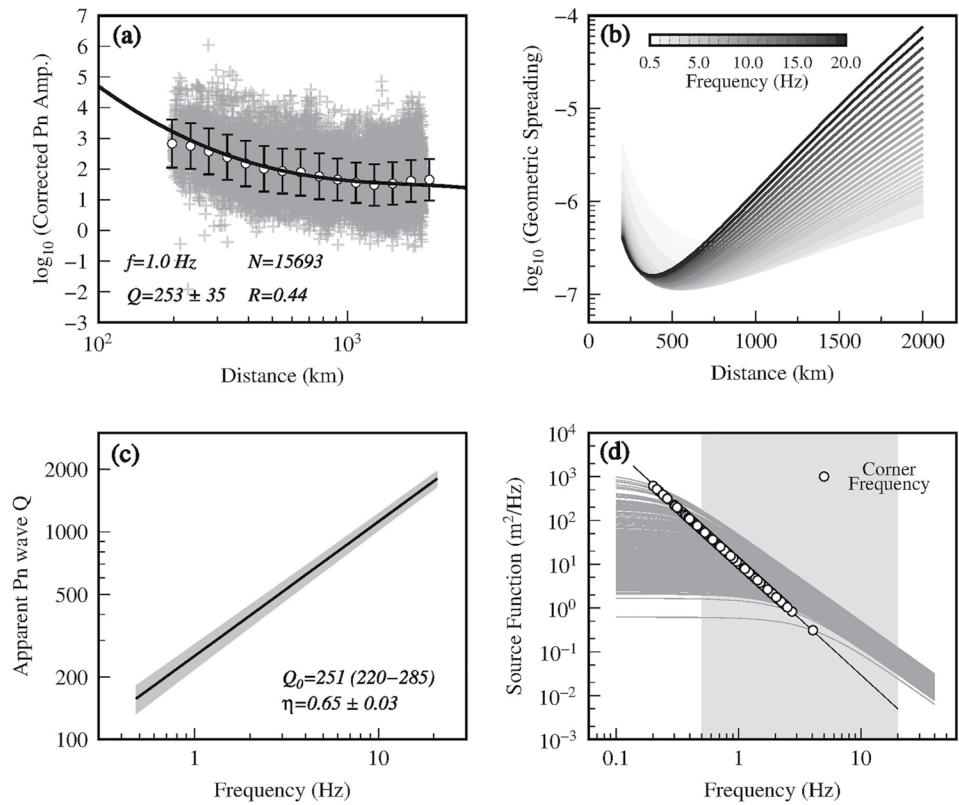


Figure 3. The inverted Pn models. (a) Corrected Pn spectral amplitudes (gray crosses) versus distance at 1.0 Hz. A total of 15,693 Pn amplitudes were corrected by removing their source excitation spectra. The black error bars are the logarithmic standard deviations of the amplitude data. The synthetic Pn spectra (solid black line) were obtained by fitting the geometric spreading, the source functions, and the regional apparent Q_{Pn} . The frequency (f), number of samples (N), apparent Pn Q , and correlation coefficient (R) are labeled. (b) Pn geometric spreading functions between 0.5 and 20.0 Hz. (c) Regional average apparent Q_{Pn} model. The attenuation parameters of Q_0 and η satisfied a power-law model $Q_{Pn} = 251f^{0.65}$. (d) Source excitation functions for 594 events.

The nine geometric spreading parameters ξ_{ij} , the seismic moment M_0 , and corner frequency f_c of the 594 events are listed in Tables S2 and S3 in Supporting Information S2, and their standard deviations were calculated by randomly selecting 80% of the amplitude data and performing fitting 100 times (Efron, 1983).

2.4. Q_{Pn} Inversion

Due to the finite frequency and interference of multiple diving waves refracted at the underside of the Moho discontinuity, the Pn energy concentrates near the uppermost mantle, with the potential to penetrate several tens of kilometers below the Moho (Hill, 1973; Sereno & Given, 1990; X. B. Xie & Lay, 2017). A Pn-wave raypath can be divided into three parts, including two parts in the crust below the source and station and the part along the uppermost mantle (Figure S2 in Supporting Information S1). Therefore, the single-station attenuation integral along the Pn raypath can be expressed as

$$B(\Delta, f) = \int_{AE} \frac{ds}{Q_s} + \int_{EF} \frac{ds}{Q(x, y, f)} + \int_{FB} \frac{ds}{Q_r}, \quad (5)$$

where AE and FB represent the crustal legs of the Pn-wave at the source and station sides, respectively, and EF represents the uppermost mantle leg. From Equation 1, neglecting the influence of the site response $P(f)$ and random amplitude $r(f)$, we have

$$A(f)G^{-1}(\Delta, f) \cdot S^{-1}(f) = [\Gamma_s(AE, f)\Gamma_r(FB, f)] \cdot \exp\left[\frac{\pi f}{\alpha_2} \int_{EF} \frac{ds}{Q(x, y, f)}\right], \quad (6)$$

where $A(f)$ and $G(\Delta, f)$ can be obtained from the Pn data and the geometric spreading function, and the attenuation term $\exp\left[\frac{\pi f}{\alpha_2} \int_{EF} \frac{ds}{Q(x, y, f)}\right]$ is our target. The $\Gamma_s(AE, f)$ and $\Gamma_r(FB, f)$ represent the attenuation terms along the crustal paths near the source and station, respectively. The $[\Gamma_s(AE, f)\Gamma_r(FB, f)]$ is assumed to be a constant over the studied region and can be inverted from the data. This is because, first, it is difficult to simultaneously solve these two terms and the attenuation term for the uppermost mantle (i.e., the EF part) from only the amplitude decay along the Pn-wave raypath. Second, the lateral extents of the crustal legs AE and FB are limited compared with the EF part along the uppermost mantle (Figure S2 in Supporting Information S1), and considering the crustal attenuation as a constant has a negligible impact on the final imaging result (G. Yang et al., 2022; Zhao et al., 2015). The single-station objective function is formed from Equation 6, and we make the right-hand side of the equation approach the left-hand side by optimizing the Q_{Pn} model. Notably, the sum of all logarithmic site responses $\sum_{i=1}^N \ln P_i$ can be assumed to be zero (Ottmöller et al., 2002). Therefore, a two-step method was conducted. We first assume the sum of the perturbation of site responses $\sum_{i=1}^N \delta \ln P_i = 0$ in logarithmic form and inverted the attenuation and source terms simultaneously. After obtained the attenuation and source terms, we control a relative variation of the site responses, and the unsolved residuals were then pushed into the site term P . The site response is simply a multiplicative factor that controls the near-station amplification due to local Earth structure. Unlike the attenuation along the path of crustal leg $\Gamma_r(FB, f)$, the site terms did not exhibit a strong correlation with seismic structures. In fact, the site response is probably a very local effect (almost in the upper 30 m) and can vary over extremely short distances (e.g., Pasyanos et al., 2009). The resulting site responses range from -1.0 to 1.0 in the logarithmic domain (Figure S3 in Supporting Information S1).

For two stations i and j that recorded the same event at different epicentral distances and similar azimuth directions ($<15^\circ$), their spectral ratio can be expressed as

$$A_{ij} = \frac{A_j(f)}{A_i(f)} = \frac{G(\Delta_j, f) \Gamma_s(AE_j, f) \Gamma(EF_j, f) \Gamma_r(FB_j, f) P_j(f) \cdot r_j(f)}{G(\Delta_i, f) \Gamma_s(AE_i, f) \Gamma(EF_i, f) \Gamma_r(FB_i, f) P_i(f) \cdot r_i(f)} \quad (7)$$

where the common source term has been eliminated. The attenuation terms in the source-side and station-side crustal legs are $\frac{\Gamma_s(AE_j, f)}{\Gamma_s(AE_i, f)} = 1$ and $\frac{\Gamma_r(FB_j, f)}{\Gamma_r(FB_i, f)} \approx 1$, respectively. Therefore, the objective function for the two-station amplitude ratio can be further expressed as

$$A_{ij}(f) \frac{G(\Delta_i, f)}{G(\Delta_j, f)} = \exp\left[-\frac{\pi f}{\alpha_2} \int_{F_i}^{F_j} \frac{ds}{Q(x, y, f)}\right]. \quad (8)$$

Combining two-station amplitude ratios and single-station amplitude data can effectively mitigate the trade-off between source and attenuation, while increasing raypath density to enhance the resolution and reliability of attenuation imaging. At each frequency, a constant Q model calculated from the amplitude ratio data is used as the initial model for inversion. We linearize Equations 6 and 8 in the logarithmic domain to establish the single- and two-station inversion systems

$$\begin{bmatrix} \mathbf{H}_s \\ \mathbf{H}_t \end{bmatrix} = \begin{bmatrix} \mathbf{A}_s \\ \mathbf{A}_t \end{bmatrix} \cdot \delta \mathbf{Q} + \begin{bmatrix} \mathbf{E} \\ 0 \end{bmatrix} \cdot \delta \mathbf{S}, \quad (9)$$

where \mathbf{H}_s is a vector composed of residuals between the observed and synthesized Pn spectra, \mathbf{H}_t is the residual vector between observed and synthetic spectral ratios, $\delta \mathbf{Q}$ is the perturbation of Q_{Pn} , $\delta \mathbf{S}$ is the perturbation of the logarithmic Pn source function, and the matrices $\mathbf{A}_{s,t}$ and \mathbf{E} set up the relationships between $\delta \mathbf{Q}$ and $\mathbf{H}_{s,t}$ and between $\delta \mathbf{S}$ and $\mathbf{H}_{s,t}$, respectively. Single-station amplitude and two-station amplitude ratio equations are jointly solved by the least squares orthogonal factorization inversion method (Paige & Saunders, 1982) to obtain the distribution of the Pn-wave quality factor (Q_{Pn}) after removing the influence of the source, radiation pattern and geometric spreading. The turning point of the L-curve was selected as the optimal initial damping parameter in Q_{Pn} tomography to balance data fitting with the preservation of robust anomaly features. Subsequent iterations employed varying damping values to refine the data fit while maintaining the integrity of the anomaly features. As the number of iterations increases, the damping value decreases gradually (G. Yang et al., 2023). During the tomographic inversion, the amplitude residuals become narrower, sharper, have a zero mean, and are gradually closer to Gaussian distributions (Figure 4). Checkerboard tests at individual frequencies were conducted

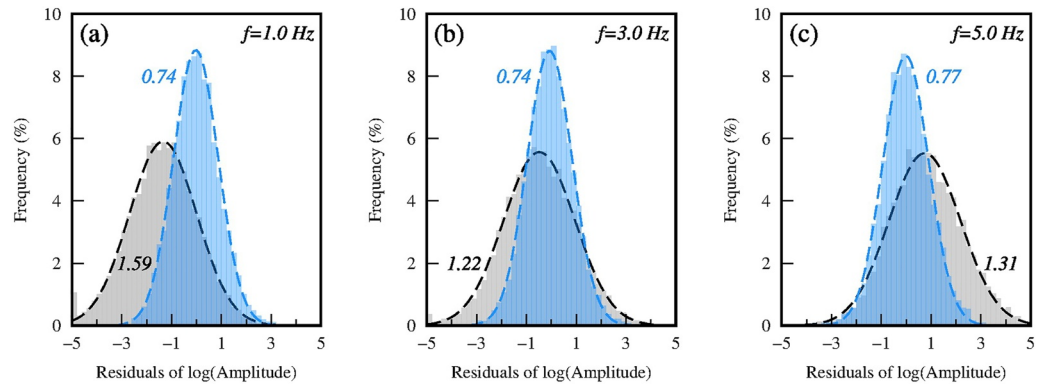


Figure 4. Histograms of the Pn spectral amplitude misfits before (gray) and after (blue) inversions at 1.0, 3.0, and 5.0 Hz. The dashed lines represent the best-fitting normal distribution curves. The root-mean-square (rms) residuals before and after inversions are labeled.

to analyze the resolution and reliability of the inversion system, where the checkerboards were constructed by adding 7% positive/negative perturbations over a constant background Q_{p_n} model (Zhao et al., 2015). For detailed Pn attenuation tomography methodology, refer to Zhao et al. (2015) and G. Yang et al. (2022).

3. Results

3.1. Tomographic Attenuation Model of Pn-Wave

A high-resolution Pn-wave attenuation model was constructed for the Iranian Plateau at 42 individual frequencies between 0.5 and 20.0 Hz. Lateral variations in the Pn attenuation are remarkable, as shown in the selected Q_{p_n} images at 1.0, 2.0, 3.0, and 5.0 Hz (Figure 5). With dense ray paths, the synthesized Pn spectral amplitudes can well recover the $1.0^\circ \times 1.0^\circ$ checkerboard models at individual frequencies (Figure 6). The large-scale attenuation structures are generally stable at individual frequencies, and the Q_{p_n} value increases with frequency. Based on the Pn attenuation model, the Q_{p_n} value versus frequency is statistically obtained in six major geological units, including the Eurasian and Arabian Plates, the Afghan block, and the Iranian, Pamir, and Anatolian Plateaus (Figure S4 in Supporting Information S1). The Q_{p_n} -frequency curves seem to be parabolas between 0.5 and 20.0 Hz, where the Anatolian and Iranian Plateaus exhibit relatively lower Q_{p_n} values. Comparing the frequency dependencies of different units, the portion between 0.5 and 5.0 Hz can clearly distinguish different units (Figure 7a and Figure S4h in Supporting Information S1). However, outside of the dominating band, the Q_{p_n} curves are mixed closer and strongly dependent on frequency rather than tectonic features. Therefore, the frequency range from 0.5 to 5.0 Hz was selected as the dominant band for the Pn attenuation model.

The broadband attenuation model was calculated by the logarithmic average of Q_{p_n} values between 0.5 and 5.0 Hz (Figure 7b). The lateral variation in broadband Pn attenuation closely resembles that observed at individual frequencies (Figure 5), and it also demonstrates a high degree of consistency with previous attenuation and velocity imaging results for the uppermost mantle (see Section 4.1). The broadband Q_{p_n} value extends from 10 to 700, where the Arabian Plate, the Eurasia Plate and the Makran subduction region are characterized by weak attenuation in the uppermost mantle ($Q_{p_n} > 500$) and high velocities from previous tomographic results (e.g., Al-Lazki et al., 2014; Amini et al., 2012; Lü et al., 2012, 2017; Pei et al., 2011). From west to east, the Anatolian Plateau, the Iranian Plateau, the Afghan Block and the Pamir Plateau exhibit overall lower Q_{p_n} ($Q_{p_n} < 250$), which is aligned with the Pn low-velocity anomalies (e.g., Al-Lazki et al., 2014; Amini et al., 2012; Lü et al., 2017; Pei et al., 2011). With contributions from the new CIGSIP stations, dense raypath coverage, and accurate measurement of Pn amplitude, more details were discovered in our high-resolution Pn attenuation model. Inside the Iranian Plateau (Figure 7c), the high- Q_{p_n} values observed in the uppermost mantle beneath the Zagros orogen are indicative of the cold Arabian continental lithosphere. Within this region, the northwestern and southeastern parts exhibit significantly higher Q_{p_n} values compared to the middle part, and they extend further to the northeast (H1 and H2). Along the UDMA, two low- Q_{p_n} anomalies are revealed beneath the northwestern end near the Alborz Mountains and the southeastern UDMA near the Makran region (L1 and L2). The Alborz and Kopet-Dogh

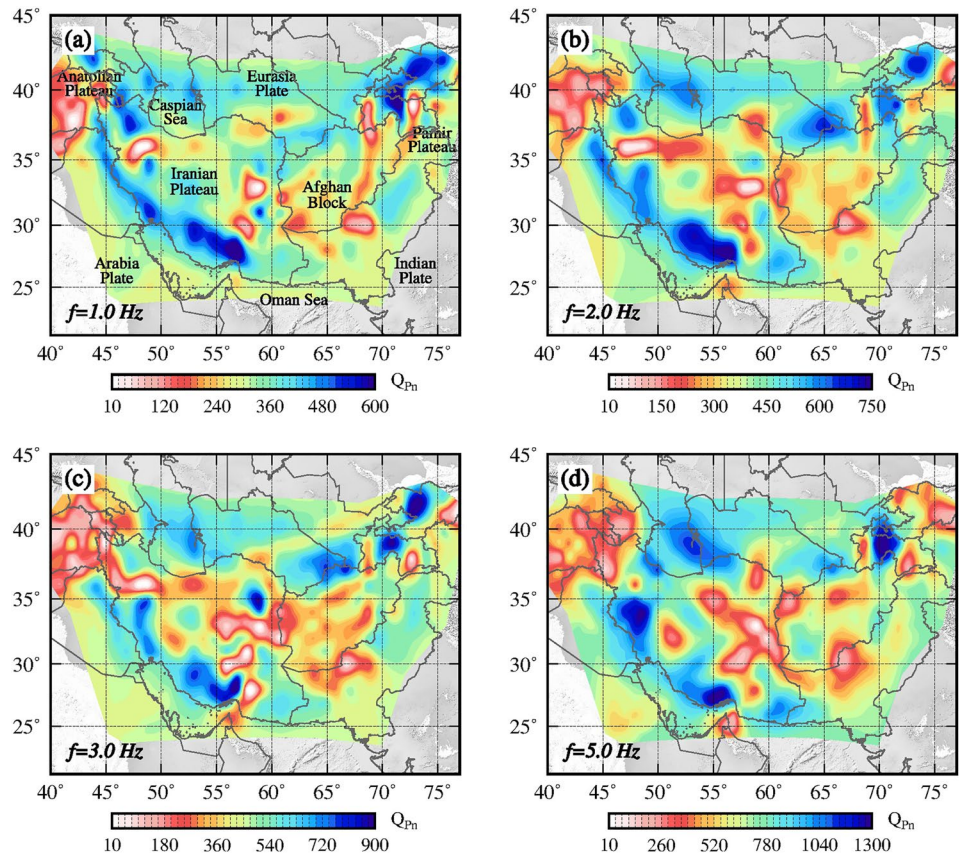


Figure 5. Selected Q_{p_n} images at 1.0, 2.0, 3.0, and 5.0 Hz, respectively.

Mountains show low- Q_{p_n} features and crop out in the Alborz volcanic rocks. Similarly, strong Pn attenuation was observed beneath the Lut magmatic zone (LMZ) in the eastern Iranian Plateau.

3.2. Uncertainty Analysis and Synthetic Tests

The uncertainty of results from the observations can be examined by resampling the original data set using the bootstrapping technique (Efron, 1983). Repeatedly reconstructing the attenuation model 100 times, each time randomly selecting 80% of the ray paths from the entire single- and two-station observational data sets, we generated a map of mean Q_{p_n} values with small standard deviations ($SD < 60$). This map closely resembles the directly inverted Q_{p_n} map (Figure S5 in Supporting Information S1), demonstrating the robustness of our approach. A synthetic test is further performed to confirm whether the main structural features under the Iranian Plateau are robust. As shown in Figure S6a in Supporting Information S1, the input model includes two high- Q_{p_n} anomalies in the Zagros (H1 and H2) and a low- Q_{p_n} anomaly in the southeastern UDMA (L1). The background is the average Q_{p_n} value of this region, and the attenuation anomalies are set to $\pm 50\%$ perturbations. The synthetic amplitudes are generated from the theoretical models based on Equation 1, given the source and geometric spreading terms. Introducing 5% random noise into the data revealed that the main structural features remain robust, and both the shapes and magnitudes of the given anomalies can be successfully recovered (Figure S6b in Supporting Information S1). Otherwise, the effects of uneven station distribution on tomography were also examined in a previous Lg-wave attenuation study (G. Yang et al., 2023). The test results indicate that the CIGSIP stations enhance the constraints on the attenuation structure between the two dense networks and do not produce synthetic anomalies.

4. Discussion

4.1. Comparison With Previous Studies

The crustal Lg-wave attenuation was investigated in and around the Iranian Plateau using the same data set (Figure 7d) (G. Yang et al., 2023). Low crustal Q_{L_g} and high uppermost mantle Q_{p_n} values are observed beneath

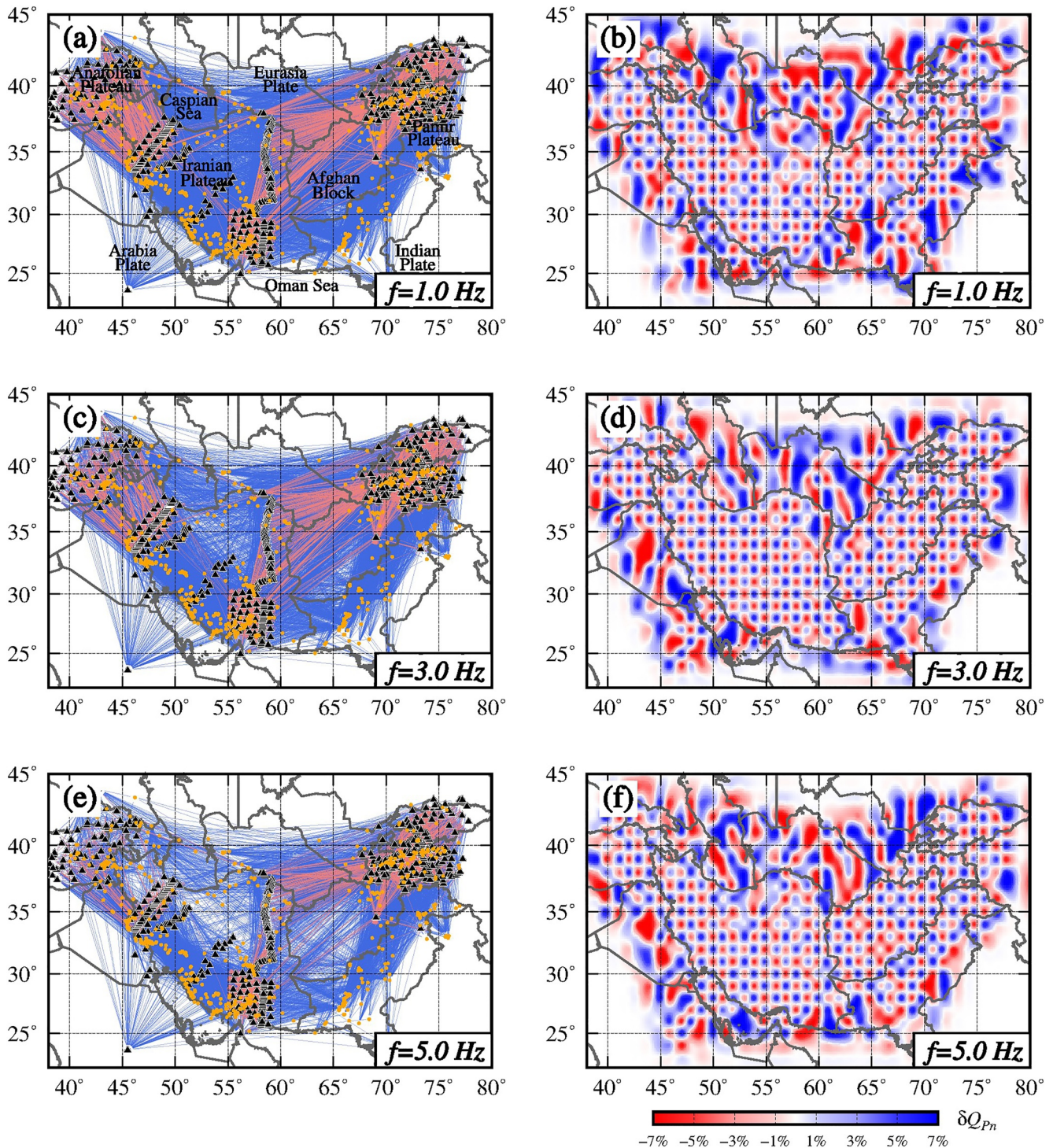


Figure 6. Raypath coverages and checkerboard resolution analyses at 1.0, 3.0, and 5.0 Hz. The blue and red lines represent the single-station and double-station paths, respectively. Black triangles and orange circles denote the stations and events used in this study, respectively.

the Zagros orogen and are related to the active crustal deformation and cold plate underthrusting, respectively. Kreemer et al. (2014) presented a global strain rate model, where the higher strain rate is mainly localized in the northern and southern Iranian Plateau, including the Zagros orogen. The decreasing GPS velocity observed from the Zagros orogen to the northern Iranian Plateau also supported that the Zagros orogen is experiencing intense crustal deformation (e.g., Khorrani et al., 2019). This is consistent with the low- Q_{Lg} feature and the previously

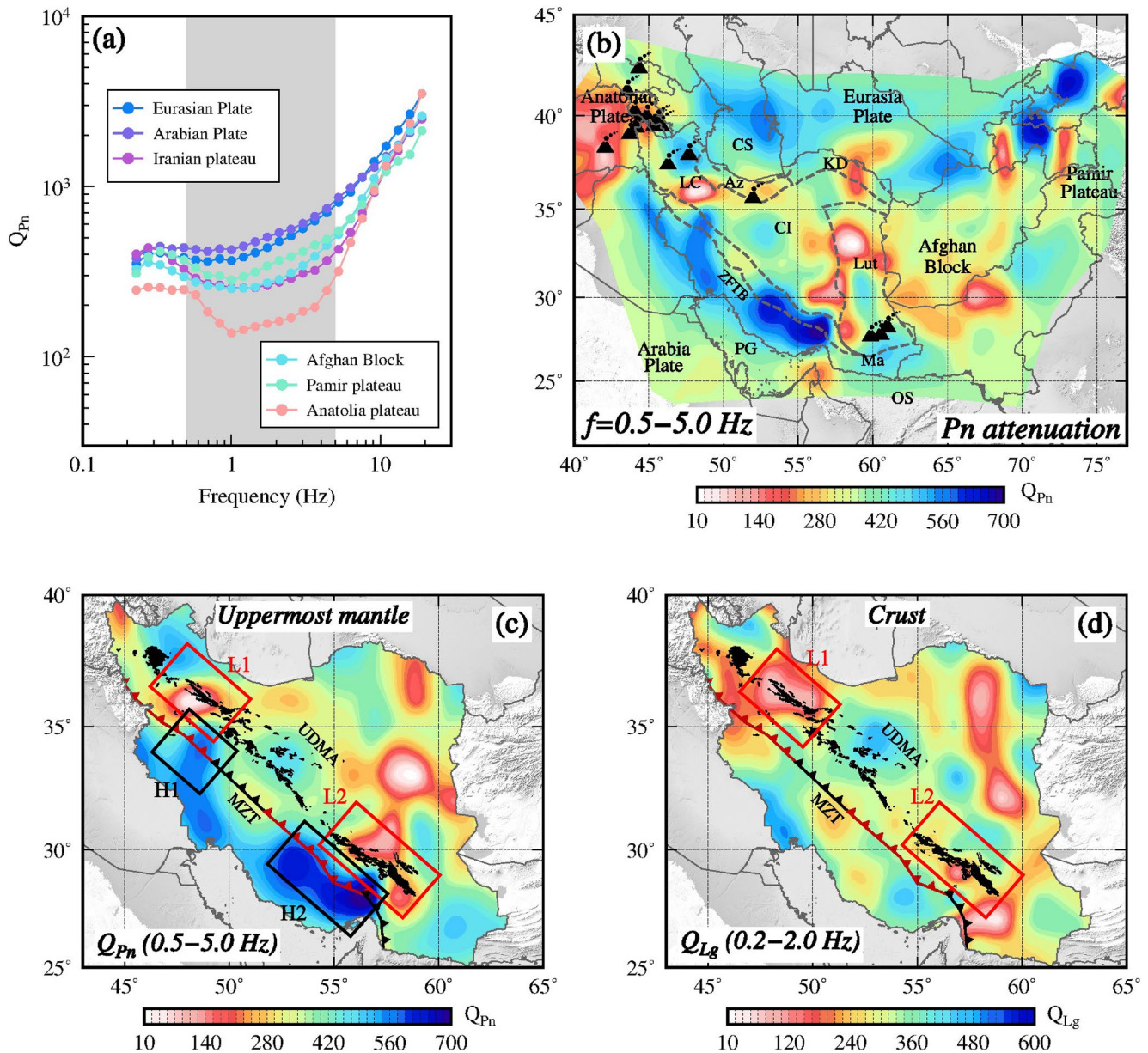


Figure 7. Maps showing broadband Pn-wave attenuation tomographic results. (a) Comparison of the frequency-dependent Q_{Pn} of selected blocks (Figure S4 in Supporting Information S1). The shaded areas highlight the dominating frequency band of 0.5–5.0 Hz. (b) Broadband Q_{Pn} map (logarithmic average of Q_{Pn} from 0.5 to 5.0 Hz). The volcanoes are marked as black triangles. (c) Uppermost mantle Q_{Pn} image inside the Iranian Plateau. (d) Crustal Q_{Lg} images inside the Iranian Plateau (G. Yang et al., 2023). The black areas represent the locations of Cenozoic Urumieh-Dokhtar volcanic rock outcrops. The Main Zagros Thrust represents the suture of two continental plates, along which the Neotethys subducted beneath central Iran. The possible slab break-off regions (red segments) were suggested by results from seismic tomography and geochemical observations (Agard et al., 2011; Hafkenscheid et al., 2006; Omrani et al., 2008). The low- Q_{Pn} and low- Q_{Lg} zones L1 and L2 and the high- Q_{Pn} zones H1 and H2 are revealed beneath the Urumieh-Dokhtar magmatic arc and Zagros orogen, respectively.

observed lower b-values (Mousavi, 2017a, 2017b). Higher strain rates can indicate higher stress accumulation, hence corresponding with the intense tectonic deformation and the strong attenuation of Lg-wave amplitude. Higher susceptibility, magnetic remanence and density are also observed beneath the UDMA and the Zagros Fold-and-Thrust belt (e.g., Abedi & Oskooi, 2015; Abedi et al., 2018). Some strong attenuation anomalies can be simultaneously observed in both the uppermost mantle and crust. For example, two anomalies with crustal low- Q_{Lg} and uppermost mantle low- Q_{Pn} values are revealed beneath the northwestern and southeastern UDMA (L1 and L2 in Figures 7c and 7d), suggesting upwellings from the uppermost mantle to the crust, which is consistent with previous velocity and attenuation tomographic images (e.g., Amini et al., 2012; Hearn, 2022; Kaviani

et al., 2022; Pei et al., 2011). Additionally, the Lut magmatic belt with low- Q_{Lg} and low- Q_{Pn} values suggests magmatic accumulations in the crust and uppermost mantle (see Section 4.2 for detailed discussion).

Hearn (2022) conducted Pn attenuation tomography for the Iranian Plateau and found that the Zagros orogen is characterized by high- Q_{Pn} , the interior of the Iranian Plateau features overall low- Q_{Pn} , and the northwestern and southeastern Zagros are represented by more prominent high- Q_{Pn} anomalies. Hearn's results are consistent with ours. Previous *P*- and *S*-wave attenuation images in the upper mantle also show a high-*Q* anomaly beneath the Zagros orogen and a low-*Q* anomaly north of the Main Zagros Thrust (Kaviani et al., 2022; Pasyanos et al., 2021). Seismic velocity tomography can reveal the temperature, melting distribution and rock composition of deep structures and has been widely applied in and around the Iranian Plateau (e.g., Alinaghi et al., 2007; Al-Lazki et al., 2004, 2014; Amini et al., 2012; Lü et al., 2012, 2017; Mahmoodabadi et al., 2019; Pei et al., 2011). The Anatolian, Iranian, and Pamir Plateaus and the Afghan Block are characterized by low Pn and Sn velocities based on previous tomographic results (Figure S7 in Supporting Information S1) (Pei et al., 2011). Low-velocity anomalies can be observed beneath Alborz Mountain and the Lut Block inside the Iranian Plateau, which are consistent with strong Pn attenuation in the uppermost mantle. The Arabian continental margin underlying the Zagros orogen invariably exhibits high Pn and Sn velocities and weak Pn attenuation features. The low-angle Makran subduction slab can be revealed by a high- Q_{Pn} and high-velocity anomaly in the uppermost mantle beneath the southeastern edge of Iran, which is parallel to the strike of the Makran Trench. The Pn velocity pattern generally aligns with the attenuation pattern in the Iranian Plateau. However, notable discrepancies arise in the finer details of the velocity and attenuation observations, particularly within the central region of the Iranian Plateau (Al-Lazki et al., 2014; Amini et al., 2012; Lü et al., 2012, 2017; Pei et al., 2011). Typically, the Arabian Plate below the Zagros orogen is characterized by obviously higher Q_{Pn} values on both the northwestern and southeastern sides (H1 and H2 in Figure 7c), which may be related to the underthrusting pattern of the Arabian Plate, as discussed in Section 4.3.

4.2. Magma Upwelling Beneath the Lut Magmatic Zone

The storage-transport processes of the ascending melt can be detected by the strong attenuation features based on the crustal and uppermost mantle attenuation models. In the Lut Block, diffuse magmatism is almost continuous from the Early Cretaceous to the Quaternary (Jentzer et al., 2020). The formation of Lut volcanism may be related to WE-dipping Sistan Oceanic subduction (e.g., Moghaddam et al., 2021; Saccani et al., 2010) and lithospheric delamination during the Lut-Afghan collision (Pang et al., 2013). A low- Q_{Lg} belt spans the northern Lut Block, the Sabzevar zone and the Kopet-Dogh Mountains. Two strong attenuation centers ($Q_{Lg} < 150$) correspond well to the LMZ and the Alborz magmatic belt (Figure 8). Similarly, Pn attenuation reveals two magmatic sources ($Q_{Pn} < 250$) in the uppermost mantle. The geochemical analyses support that the magmatic source of the late Paleocene to Oligocene volcanism was in the upper mantle and further modified by crustal components (Pang et al., 2013). The attenuation model further suggests that the younger volcanism in the Lut and Alborz magmatic zones is mainly fed by two potential asthenospheric upwellings, possibly originating from the deep asthenospheric low-velocity layer at ~100–150 km depth beneath eastern Iran (Wu et al., 2021; G. Yang et al., 2023). The two magma upwellings gradually merge and are difficult to distinguish in the crust (G. Yang et al., 2023). Younger Pliocene-Quaternary igneous rocks and ocean island basalt (OIB)-type outcrops suggest that high-temperature melts gathered beneath the northeastern Iranian Plateau (Su et al., 2014; Walker et al., 2009).

4.3. Segmented Up-Bending/Underplating of the Arabian Continental Plate

The Arabian continental underthrusting followed the subduction of the Neotethyan oceanic lithosphere into the trench. Upper mantle *P*- and *S*-wave velocity tomography revealed high-velocity anomalies down to a 600 km depth beneath Iran (e.g., Alinaghi et al., 2007; Hafkenscheid et al., 2006; Mahmoodabadi et al., 2019; Manaman & Shomali, 2010; Rahmani et al., 2019; Veisi et al., 2021), where the shallower high-velocity anomaly (<200 km) was interpreted as the Arabian mantle lithosphere and the high-velocity anomaly below ~200 km was interpreted as the remaining Neotethyan oceanic slab. Detached slabs were detected at depths exceeding 300 km beneath the northwestern and southeastern Zagros orogen. However, beneath the central Zagros, high-velocity anomalies persisted at depths of 200–500 km, suggesting a connection to the shallower Arabian continental margin (Agard et al., 2011; Hafkenscheid et al., 2006; Rahmani et al., 2019; Veisi et al., 2021). Therefore, the subducted deep slab was proposed to be partially detached under the Iranian Plateau (red dashed lines in Figure 9a). According

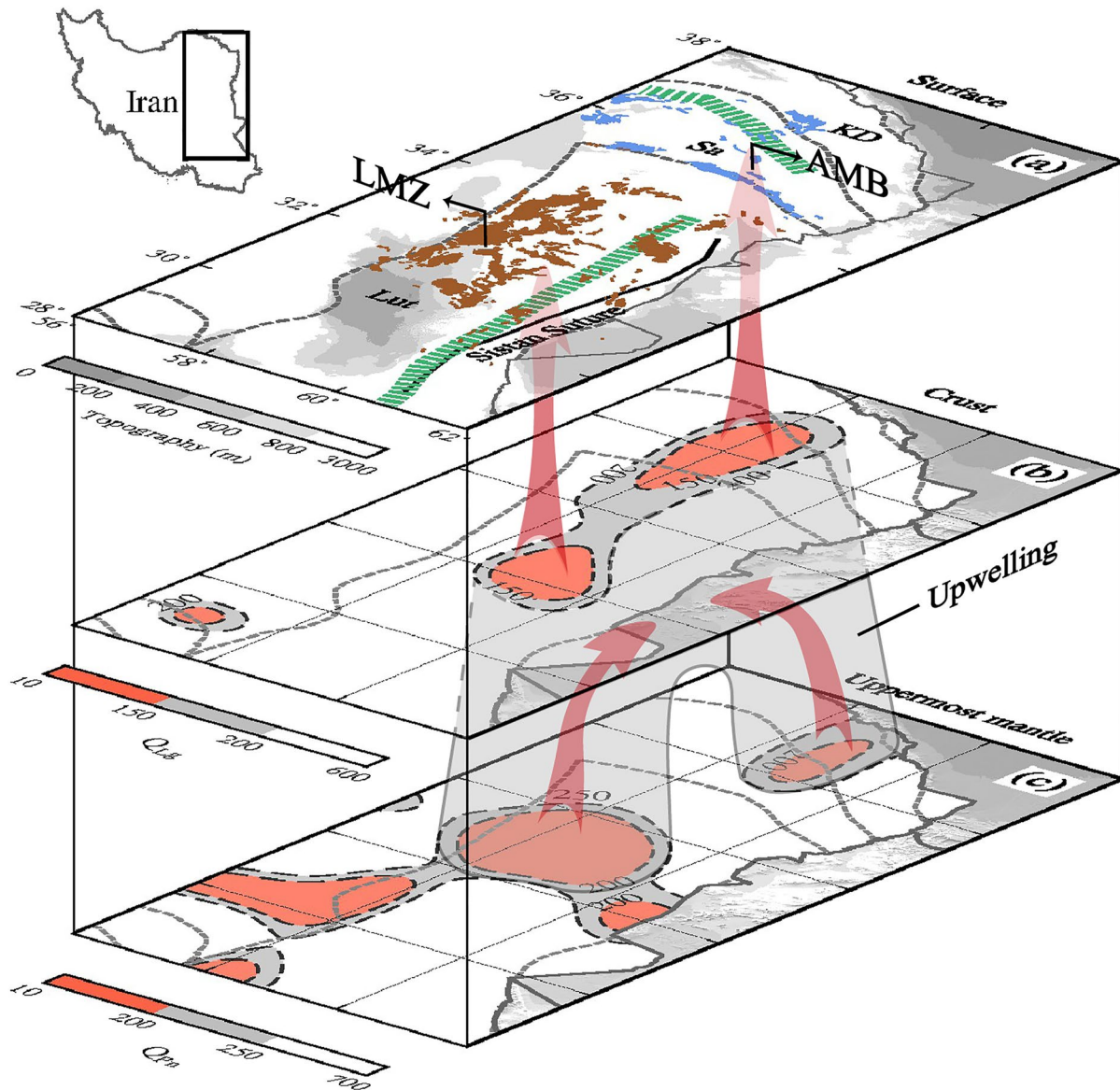


Figure 8. Broadband Q_{Lg} and Q_{Pn} maps of the Lut Block. (a) Topographic map near the Lut Block. The green bands on the map represent the Cretaceous ophiolite belts. The brown and blue fills represent the Lut magmatic zone and the Alborz magmatic belt. Sa = Sabzevar zone; KD = Kopet-Dogh Mountains; and Lut = Lut Block. (b) Distribution of crustal low- Q_{Lg} anomalies ($Q_{Lg} < 200$). (c) Distribution of low- Q_{Pn} anomalies in the uppermost mantle ($Q_{Pn} < 250$). Red arrows indicate potential magmatic upwellings.

to the ages of the adakitic rocks, the slab break-off occurred during ~ 40 – 30 Ma under northwestern Iran, skipped central Iran, and propagated southeast to Makran from 10 to 5 Ma to the present (Agard et al., 2011; Hafkenscheid et al., 2006; Omrani et al., 2008). However, the detachment locations from different velocity tomographic images were not uniform (e.g., Mahmoodabadi et al., 2019). These disputes may be resolved by the characteristics of the shallower continental lithosphere.

The breaking of a subducted slab has profound impacts on the thermal structure of the mantle wedge. The possible slab break-off regions are highlighted using the red dashed lines in Figure 9a (Agard et al., 2011; Alinaghi et al., 2007; Omrani et al., 2008). The slab detachment zones beneath the northwestern and southeastern Zagros are consistent with convex high- Q_{Pn} anomalies in the uppermost mantle. Numerical simulations indicate that after slab break-off at depth, the subducted continental plate will rise back or up-bend toward the surface under the action of buoyancy at shallower depths and further flatten below the overriding plate (Figure S8 in Supporting Information S1) (e.g., Li et al., 2013; Magni et al., 2017; van Hunen & Allen, 2011). Compared to the central

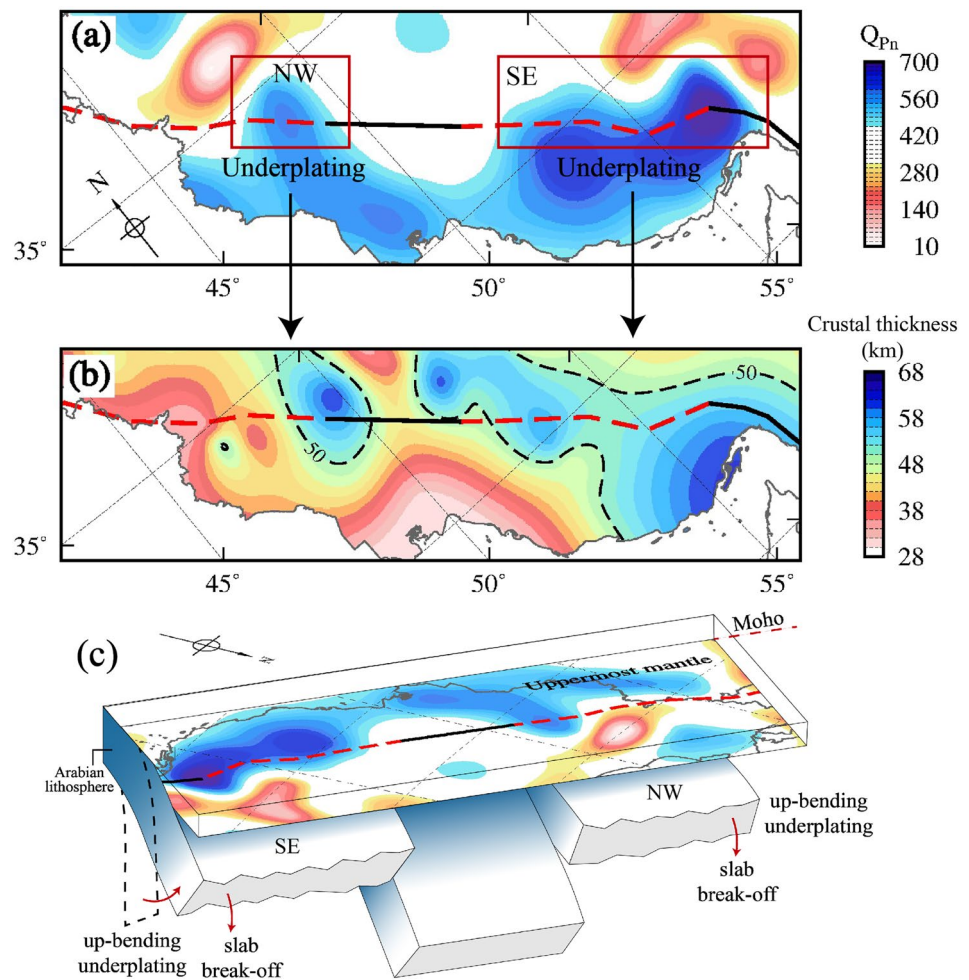


Figure 9. Plate up-bending/underplating zones inferred by P_n attenuation. (a) The Q_{Pn} image beneath the Zagros orogen. The black solid and red dashed lines represent the suture of two continental plates, along which the Neotethys subducted beneath central Iran, where the red dashed segments represent the possible slab break-off regions (Agard et al., 2011; Alinaghi et al., 2007; Omrani et al., 2008). Two possible up-bending zones of the Arabian Plate are circled in red frames. (b) Crustal thickness map from Taghizadeh-Farahmand et al. (2015). Northwestern and southeastern Zagros with high- Q_{Pn} values both correspond to thicker crusts. (c) Schematic diagram showing slab break-offs and continental plate up-bending under the Zagros orogen.

Zagros, the northwestern and southeastern segments of the Arabian lithosphere, characterized by stronger high- Q_{Pn} anomalies, extend further in the direction of underthrusting. This observation aligns well with the proposed plate up-bending process and suggests that the Arabian Plate may have bent upward above the detached slabs, causing the high- Q_{Pn} anomalies to extend forward near the Moho (Figure 9c). The rising of the subducted continental crust forces the mantle wedge to progressively migrate away from the trench (Magni et al., 2017). Beneath the Zagros orogen, the northwestern and southeastern Arabian Plates with high- Q_{Pn} migrate as far as ~ 150 and ~ 70 km north of the main suture during approximately 30 and 10 Myr (Omrani et al., 2008), respectively, which aligns with the migration velocity of ~ 200 km/35 Myr suggested by numerical simulation (Magni et al., 2017).

The Moho depth map obtained from the receiver function showed thicker crusts (>50 km) beneath northwestern and southeastern Zagros (Mooney, 2015; Taghizadeh-Farahmand et al., 2015), which corresponded to the stronger high- Q_{Pn} anomalies and the possible plate up-bending zones of the Arabian lithosphere (Figure 9b). Furthermore, the thicker crustal structures in northwestern and southeastern Zagros were also supported by other Moho models based on surface wave tomography (Kaviani et al., 2020; Manaman et al., 2011), despite some differences. This indicated that, following the slab break-off, the upward bending and forward underthrusting of the continental lithosphere can generate high compressional stresses to the overlying crust, leading to

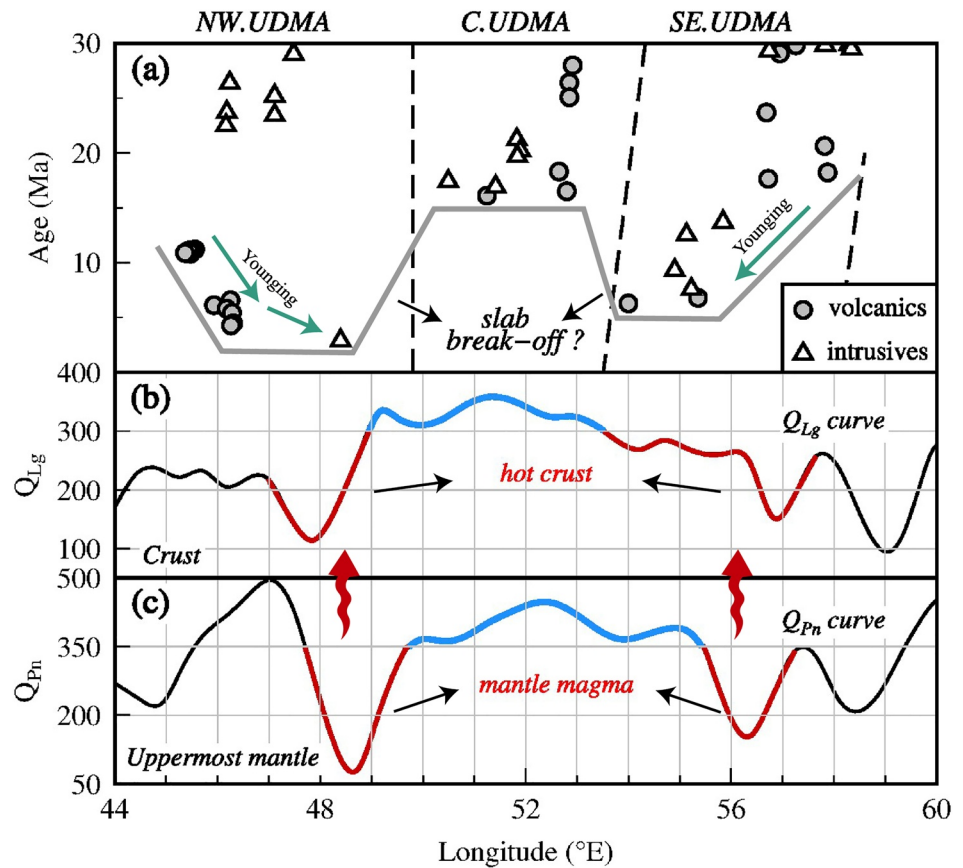


Figure 10. Distributions of magmatic rock ages and attenuation Q along the Urumieh-Dokhtar magmatic arc (UDMA). (a) Age versus space plot of dated samples from the UDMA, modified from Chiu et al. (2013). The solid line outlines the age variation in young volcanism. The green arrows indicate the younging directions of magmatism. (b, c) Q_{Lg} and Q_{Pn} curves along the UDMA. The weak and strong attenuation zones are shown in blue and red, respectively. The red arrows suggest potential mantle upwelling related to slab break-off.

further crustal thickening of the northwestern and southeastern Zagros. Various studies have demonstrated slab detachment and plate underplating occurred beneath the northwestern and southeastern Zagros orogen (Agard et al., 2011; Alinaghi et al., 2007; Hafkenscheid et al., 2006).

4.4. Detachment-Related Mantle Upwelling

Spanning approximately 1,500 km along the continental underthrusting front, the UDMA is a linear magmatic belt that bears the imprint of subduction-related processes. From the Late Cretaceous to the Paleogene, the UDMA witnessed prolific eruptions of low-K tholeiitic and calc-alkaline magmas, resulting in extensive volcanic successions with minor intrusive rocks (Chiu et al., 2017). The Eocene–Oligocene volcanoes in the UDMA were fed by the mantle wedge melting induced by the Neotethys subduction (e.g., Asadi et al., 2014), but the formation mechanism of late Cenozoic magmatism is controversial. Several interpretation models have been proposed, including slab rollback (e.g., Babazadeh et al., 2017), slab break-off (e.g., Ghalamghash et al., 2016; Jahangiri, 2007; Omrani et al., 2008), changes in subduction angle (Shahabpour, 2007), and crustal thickening (Chiu et al., 2013).

Figure 10a illustrates the age distribution of igneous rocks along the UDMA (Chiu et al., 2013 and references herein). The magmatism in the central UDMA ceased after ~ 15 Ma, while the volcanism in the northwestern and southeastern UDMA continued to the Quaternary. In the crust, two low- Q_{Lg} zones are revealed beneath the northwestern and southeastern UDMA, and a high- Q_{Lg} zone appears around the central UDMA (Figure 7d). Similarly, two low- Q_{Pn} characteristics are shown in the uppermost mantle but have a certain shrinkage compared

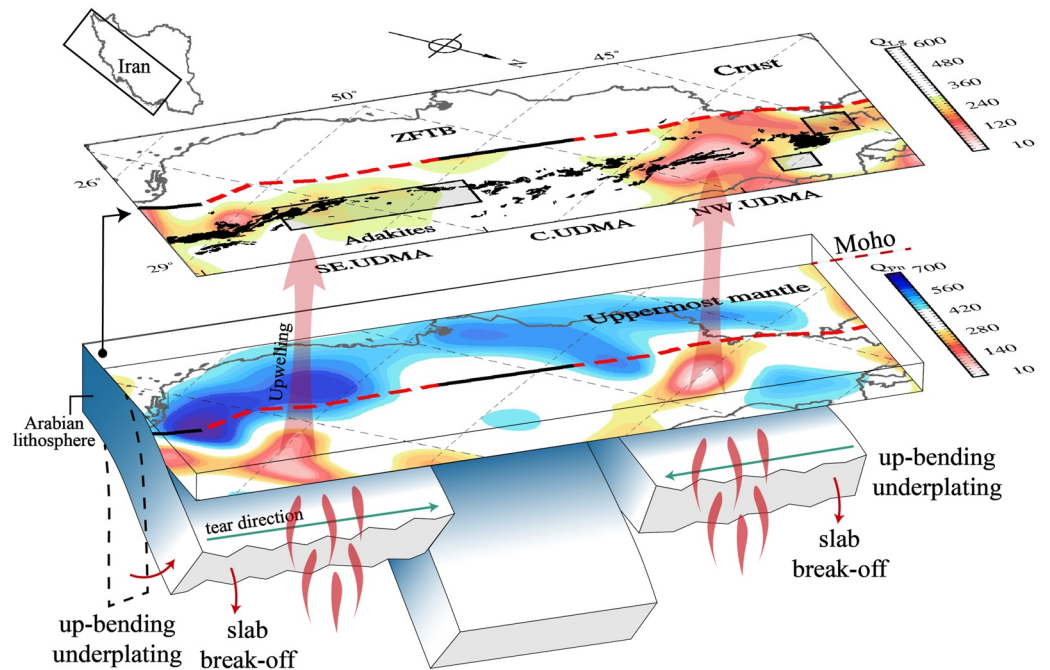


Figure 11. Schematic diagram showing the dynamics of slab break-offs, plate up-bending, and magmatic upwellings beneath the Urumieh-Dokhtar magmatic arc (UDMA). Broadband Q_{Lg} and Q_{Pn} maps are shown above and below, respectively. In the crustal attenuation map, the Cenozoic volcanic rock outcrops in the UDMA are filled as black areas. Adakitic rocks were observed in the northwestern and southeastern UDMA and marked as shaded areas (Ghalamghash et al., 2016; Jahangiri, 2007; Omrani et al., 2008). The Main Zagros Thrust (black lines and red dashed lines) represents the suture of two continental plates, along which the Neotethys subducted beneath central Iran. The red dashed segments represent the possible slab break-off regions (Agard et al., 2011; Alinaghi et al., 2007; Omrani et al., 2008). The red arrows indicate that two mantle upwellings escaped upward from slab tears and intruded into the upper mantle and crust to feed the younger volcanism at the surface.

to the crustal strong attenuation anomalies (Figure 7c). As illustrated in Figures 10b and 10c, both the Q_{Lg} and Q_{Pn} curves along the UDMA exhibit two remarkably strong attenuation zones, indicating potential magmatic accumulations. The lower velocity zones near the northwestern and southeastern UDMA were also revealed in previous Pn and Sn velocity tomography (e.g., Al-Lazki et al., 2004; Pei et al., 2011). The lateral variations observed in the thermal structure beneath the UDMA suggest intricate origins for the younger magmatism. From northwest to southeast, the young-old-young age pattern exhibited by the igneous rocks aligns remarkably with the strong-weak-strong attenuation feature, the continental plate up-bending zones, and the slab break-off regions. Therefore, the Miocene-Quaternary volcanism in the northwestern and southeastern UDMA may have been triggered by slab detachment at depth (Ghalamghash et al., 2016; Jahangiri, 2007; Omrani et al., 2008). The low- Q_{Lg} and low- Q_{Pn} anomalies imply two possible magma channels under the northwestern and southeastern UDMA (Figures 10b and 10c). The two asthenospheric upwellings escaped upward from the slab tears, intruded into the upper mantle and crust, and further fed the younger volcanism at the surface. However, the magmatism in the central UDMA has not been reactivated by a detachment-related magmatic source since ~15 Ma. Geochemical surveys also found adakitic magmas in the northwestern and southeastern UDMA in response to the melting of mafic material at depth under high-temperature conditions and possible slab break-off (Ghalamghash et al., 2016; Jahangiri, 2007; Omrani et al., 2008). Crustal thickening may also lead to magma compositional changes from calc-alkaline to adakitic (e.g., Chiu et al., 2013). However, the two magmatic sources in the uppermost mantle are distributed in clusters rather than along the collision strike, suggesting the younger magmatism was likely fed by mantle upwelling (Figure 11).

The migrations of Miocene-Quaternary volcanism are clearly identifiable in the UDMA. The volcanic rocks in the northwestern and southeastern UDMA become younger toward the central UDMA (green arrows in Figures 10a and 11). Volcanism migrations with different directions are difficult to explain in a steady-state subduction scenario or a simple oblique continental collision (e.g., Ferrari, 2004; Wortel & Spakman, 2000).

If slab break-off is used to interpret the formation of the post-collision volcanism, the along-arc migration of magmatism may support the southeastward and northwestward propagations of the slab tears beneath the northwestern and southeastern Zagros orogen (Li et al., 2013; van Hunen & Allen, 2011). Similar migration phenomena of break-off and volcanism have also been observed in multiple places, such as the northeastern Tibetan Plateau and central Mexico (Ferrari, 2004; H. Yang et al., 2021).

5. Conclusions

Combining high-resolution Pn and Lg attenuation models and other observations, we proposed the dynamic processes of slab break-off, plate up-bending/underplating and associated magmatism beneath the transition zone from the Neotethyan subduction to the Arabian collision (Figure 11). Beneath the Zagros orogen, the high- Q_{Pn} anomalies described the boundary of the Arabian underthrusting front near the Moho discontinuity, where the northwestern and southeastern parts extended farther toward the underthrusting direction, which corresponded to slab detachment zones suggested by results from seismic tomography and adakitic rocks (e.g., Agard et al., 2011; Hafkenscheid et al., 2006; Omrani et al., 2008). This indicated that after the potential slab break-offs, the northwestern and southeastern Arabian Plates rose back toward the surface under the action of buoyancy at shallower depths. The Arabian Plate further flattens below the overriding plate and forms thick crust structures (>50 km) beneath the northwestern and southeastern Zagros orogen (e.g., Taghizadeh-Farahmand et al., 2015). Affected by continental plate up-bending, the mantle wedge progressively migrated away from the suture of the Arabian and Eurasian Plates. Beneath the northwestern and southeastern UDMA, two mantle upwellings with strong attenuation features likely escaped upward from the slab tears, intruded into the upper mantle and crust and further fed the younger Miocene-Quaternary volcanism at the surface. The along-arc migration of Urumieh-Dokhtar volcanism suggests that the deep slab was likely to start breaking near the oceanic subduction zone in Makran and the eastern Mediterranean Sea and further propagated inward.

Data Availability Statement

The waveforms used in this study were collected from the Incorporated Research Institutions for Seismology Data Management Center, the German Research Centre for Geoscience, the International Seismological Centre, the International Federation of Digital Seismograph Networks, and the CIGSIP project. The Pn waveforms from the CIGSIP were uploaded to the World Data Centre for Geophysics, Beijing (WDCGB) at <http://www.geophys.ac.cn/ArticleDataInfo.asp?MetaId=503>. The single- and two-station Pn amplitude data used in this study and the resulting Pn attenuation model in the Iranian Plateau can be accessed on the WDCGB at <http://www.geophys.ac.cn/ArticleDataInfo.asp?MetaId=504> (last accessed April 2023). Certain figures were generated using Generic Mapping Tools (GMT, <https://www.generic-mapping-tools.org/>).

References

- Abedi, M., Fournier, D., Devriese, S. G. R., & Oldenburg, D. W. (2018). Potential field signatures along the Zagros collision zone in Iran. *Tectonophysics*, 722, 25–42. <https://doi.org/10.1016/j.tecto.2017.10.012>
- Abedi, M., & Oskooi, B. (2015). A combined magnetometry and gravity study across Zagros orogeny in Iran. *Tectonophysics*, 664, 164–175. <https://doi.org/10.1016/j.tecto.2015.09.003>
- Agard, P., Omrani, J., Jolivet, L., Whitechurch, H., Vrielynck, B., Spakman, W., et al. (2011). Zagros orogeny: A subduction-dominated process. *Geological Magazine*, 148(5–6), 692–725. <https://doi.org/10.1017/s001675681100046x>
- Alinaghi, A., Koulakov, I., & Thybo, H. (2007). Seismic tomographic imaging of P- and S-waves velocity perturbations in the upper mantle beneath Iran. *Geophysical Journal International*, 169(3), 1089–1102. <https://doi.org/10.1111/j.1365-246X.2007.03317.x>
- Al-Lazki, A. I., Al-Damegh, K. S., El-Hadidy, S. Y., Ghods, A., & Tatar, M. (2014). Pn-velocity structure beneath Arabia–Eurasia Zagros collision and Makran subduction zones. *Geological Society, London, Special Publications*, 392(1), 45–60. <https://doi.org/10.1144/sp392.3>
- Al-Lazki, A. I., Sandvol, E., Seber, D., Barazangi, M., Turkelli, N., & Mohamad, R. (2004). Pn tomographic imaging of mantle lid velocity and anisotropy at the junction of the Arabian, Eurasian and African plates. *Geophysical Journal International*, 158(3), 1024–1040. <https://doi.org/10.1111/j.1365-246X.2004.02355.x>
- Amini, S., Shomali, Z. H., Koyi, H., & Roberts, R. G. (2012). Tomographic upper-mantle velocity structure beneath the Iranian Plateau. *Tectonophysics*, 554–557, 42–49. <https://doi.org/10.1016/j.tecto.2012.06.009>
- Artemieva, I. M., Billien, M., Lévêque, J.-J., & Mooney, W. D. (2004). Shear wave velocity, seismic attenuation, and thermal structure of the continental upper mantle. *Geophysical Journal International*, 157(2), 607–628. <https://doi.org/10.1111/j.1365-246X.2004.02195.x>
- Asadi, S., Moore, F., & Zarasvandi, A. (2014). Discriminating productive and barren porphyry copper deposits in the southeastern part of the central Iranian volcano-plutonic belt, Kerman region, Iran: A review. *Earth-Science Reviews*, 138, 25–46. <https://doi.org/10.1016/j.earscirev.2014.08.001>
- Babazadeh, S., Ghorbani, M. R., Bröcker, M., D'Antonio, M., Cottle, J., Gebbing, T., et al. (2017). Late Oligocene–Miocene mantle upwelling and interaction inferred from mantle signatures in gabbroic to granitic rocks from the Urumieh–Dokhtar arc, south Ardestan, Iran. *International Geology Review*, 59(12), 1590–1608. <https://doi.org/10.1080/00206814.2017.1286613>

Acknowledgments

The comments from Editor M. Bostock, Associate Editor, and an anonymous reviewer are valuable and greatly improved this manuscript. This research was supported by the National Natural Science Foundation of China (91855207, 41630210, U2139206, 41974054, and 41974061). We thank M.Y. Feng for his help in preparing the waveforms from the CIGSIP stations. The CIGSIP project was implemented following the memorandum of understanding (MOU) between the Institute of Geophysics and Geology of the Chinese Academy of Sciences (IGGCAS) and the Geological Survey of Iran (GSI).

- Boyd, O. S., Jones, C. H., & Sheehan, A. F. (2004). Foundering lithosphere imaged beneath the southern Sierra Nevada, California, USA. *Science*, 305(5684), 660–662. <https://doi.org/10.1126/science.1099181>
- Chemenda, A. I., Burg, J. P., & Mattauer, M. (2000). Evolutionary model of the Himalaya-Tibet system: Geopem based on new modelling, geological and geophysical data. *Earth and Planetary Science Letters*, 174(3–4), 397–409. [https://doi.org/10.1016/S0012-821X\(99\)00277-0](https://doi.org/10.1016/S0012-821X(99)00277-0)
- Chiu, H.-Y., Chung, S.-L., Zarrinkoub, M. H., Melkonyan, R., Pang, K.-N., Lee, H.-Y., et al. (2017). Zircon Hf isotopic constraints on magmatic and tectonic evolution in Iran: Implications for crustal growth in the Tethyan orogenic belt. *Journal of Asian Earth Sciences*, 145, 652–669. <https://doi.org/10.1016/j.jseae.2017.06.011>
- Chiu, H.-Y., Chung, S.-L., Zarrinkoub, M. H., Mohammadi, S. S., Khatib, M. M., & Iizuka, Y. (2013). Zircon U–Pb age constraints from Iran on the magmatic evolution related to Neotethyan subduction and Zagros orogeny. *Lithos*, 162–163, 70–87. <https://doi.org/10.1016/j.lithos.2013.01.006>
- Davies, J. H., & Blanckenburg, F. V. (1995). Slab breakoff: A model of lithosphere detachment and its test in the magmatism and deformation of collisional orogens. *Earth and Planetary Science Letters*, 129(1–4), 85–102. [https://doi.org/10.1016/0012-821X\(94\)00237-S](https://doi.org/10.1016/0012-821X(94)00237-S)
- Efron, B. (1983). Estimating the error rate of a prediction rule: Improvement on cross-validation. *Journal of the American Statistical Association*, 78(382), 316–331. <https://doi.org/10.1080/01621459.1983.10477973>
- Ekstrom, G., Nettles, M., & Dziewonski, A. M. (2012). The global CMT project 2004–2010: Centroid-moment tensors for 13,017 earthquakes. *Physics of the Earth and Planetary Interiors*, 200, 1–9. <https://doi.org/10.1016/j.pepi.2012.04.002>
- Ferrari, L. (2004). Slab detachment control on mafic volcanic pulse and mantle heterogeneity in central Mexico. *Geology*, 32(1), 77. <https://doi.org/10.1130/g19887.1>
- Gao, Y., Chen, L., Talebian, M., Wu, Z., Wang, X., Lan, H., et al. (2022). Nature and structural heterogeneities of the lithosphere control the continental deformation in the northeastern and eastern Iranian Plateau as revealed by shear-wave splitting observations. *Earth and Planetary Science Letters*, 578, 578. <https://doi.org/10.1016/j.epsl.2021.117284>
- Gao, Y., Chen, L., Yang, J., & Wang, K. (2023). Rheological heterogeneities control the non-progressive uplift of the young Iranian Plateau. *Geophysical Research Letters*, 50(3), e2022GL101829. <https://doi.org/10.1029/2022gl101829>
- Ghalamghash, J., Mousavi, S. Z., Hassanzadeh, J., & Schmitt, A. K. (2016). Geology, zircon geochronology, and petrogenesis of Sabalan volcano (northwestern Iran). *Journal of Volcanology and Geothermal Research*, 327, 192–207. <https://doi.org/10.1016/j.jvolgeores.2016.05.001>
- Guivel, C., Morata, D., Pelleter, E., Espinoza, F., Maury, R. C., Lagabrielle, Y., et al. (2006). Miocene to Late Quaternary Patagonian basalts (46–47°S): Geochronometric and geochemical evidence for slab tearing due to active spreading ridge subduction. *Journal of Volcanology and Geothermal Research*, 149(3–4), 346–370. <https://doi.org/10.1016/j.jvolgeores.2005.09.002>
- Hafkenschied, E., Wortel, M. J. R., & Spakman, W. (2006). Subduction history of the Tethyan region derived from seismic tomography and tectonic reconstructions. *Journal of Geophysical Research*, 111(B8), B08401. <https://doi.org/10.1029/2005jb003791>
- He, X., Zhao, L. F., Xie, X. B., Tian, X., & Yao, Z. X. (2021). Weak crust in Southeast Tibetan Plateau revealed by Lg-Wave attenuation tomography: Implications for crustal material escape. *Journal of Geophysical Research: Solid Earth*, 126(3), e2020JB020748. <https://doi.org/10.1029/2020jb020748>
- Hearn, T. M. (2022). Two-dimensional attenuation and velocity tomography of Iran. *Geosciences*, 12(11), 397. <https://doi.org/10.3390/geosciences12110397>
- Hill, D. P. (1973). Critically refracted waves in a spherically symmetric radially heterogeneous earth model. *Geophysical Journal International*, 34(2), 149–177. <https://doi.org/10.1111/j.1365-246x.1973.tb02390.x>
- Jahangiri, A. (2007). Post-collisional Miocene adakitic volcanism in NW Iran: Geochemical and geodynamic implications. *Journal of Asian Earth Sciences*, 30(3–4), 433–447. <https://doi.org/10.1016/j.jseae.2006.11.008>
- Jentzer, M., Whitechurch, H., Agard, P., Ulrich, M., Caron, B., Zarrinkoub, M. H., et al. (2020). Late Cretaceous calc-alkaline and adakitic magmatism in the Sistan suture zone (Eastern Iran): Implications for subduction polarity and regional tectonics. *Journal of Asian Earth Sciences*, 204, 204. <https://doi.org/10.1016/j.jseae.2020.104588>
- Kaviani, A., Paul, A., Moradi, A., Mai, P. M., Pilia, S., Boschi, L., et al. (2020). Crustal and uppermost mantle shear wave velocity structure beneath the Middle East from surface wave tomography. *Geophysical Journal International*, 221(2), 1349–1365. <https://doi.org/10.1093/gji/ggaa075>
- Kaviani, A., Sandvol, E., Ku, W., Beck, S. L., Türkelli, N., Özacar, A. A., & Delph, J. R. (2022). Seismic attenuation tomography of the Sn phase beneath the Turkish-Iranian Plateau and the Zagros mountain belt. *Geosphere*, 18(4), 1377–1393. <https://doi.org/10.1130/ges02503.1>
- Khorrani, F., Vernant, P., Masson, F., Nilfouroushan, F., Mousavi, Z., Nankali, H., et al. (2019). An up-to-date crustal deformation map of Iran using integrated campaign-mode and permanent GPS velocities. *Geophysical Journal International*, 217(2), 832–843. <https://doi.org/10.1093/gji/ggz045>
- Kreemer, C., Blewitt, G., & Klein, E. C. (2014). A geodetic plate motion and global strain rate model. *Geochemistry, Geophysics, Geosystems*, 15(10), 3849–3889. <https://doi.org/10.1002/2014gc005407>
- Kufner, S. K., Kakar, N., Bezada, M., Bloch, W., Metzger, S., Yuan, X., et al. (2021). The Hindu Kush slab break-off as revealed by deep structure and crustal deformation. *Nature Communications*, 12(1), 1685. <https://doi.org/10.1038/s41467-021-21760-w>
- Kundu, B., & Gahalaut, V. K. (2011). Slab detachment of subducted Indo-Australian plate beneath Sunda arc, Indonesia. *Journal of Earth System Science*, 120(2), 193–204. <https://doi.org/10.1007/s12040-011-0056-7>
- Laske, G., Masters, G., Ma, Z., & Pasyanos, M. (2013). Update on CRUST1.0 – A 1-degree global model of Earth's crust. In *EGU general assembly 2013*.
- Li, Z.-H., Xu, Z., Gerya, T., & Burg, J.-P. (2013). Collision of continental corner from 3-D numerical modeling. *Earth and Planetary Science Letters*, 380, 98–111. <https://doi.org/10.1016/j.epsl.2013.08.034>
- Lü, Y., Liu, B., Pei, S., Sun, Y., Toksoz, M. N., & Zeng, X. (2012). Pn tomographic velocity and anisotropy beneath the Iran region. *Bulletin of the Seismological Society of America*, 102(1), 426–435. <https://doi.org/10.1785/0120100141>
- Lü, Y., Ni, S., Chen, L., & Chen, Q.-F. (2017). Pn tomography with Moho depth correction from eastern Europe to western China. *Journal of Geophysical Research: Solid Earth*, 122(2), 1284–1301. <https://doi.org/10.1002/2016jb013052>
- Magni, V., Allen, M. B., van Hunen, J., & Bouilhol, P. (2017). Continental underplating after slab break-off. *Earth and Planetary Science Letters*, 474, 59–67. <https://doi.org/10.1016/j.epsl.2017.06.017>
- Mahmoodabadi, M., Yaminifard, F., Tatar, M., Kaviani, A., & Motaghi, K. (2019). Upper-mantle velocity structure beneath the Zagros collision zone, Central Iran and Alborz from nonlinear teleseismic tomography. *Geophysical Journal International*, 218(1), 414–428. <https://doi.org/10.1093/gji/ggz160>
- Manaman, N. S., & Shomali, H. (2010). Upper mantle S-velocity structure and Moho depth variations across Zagros belt, Arabian–Eurasian plate boundary. *Physics of the Earth and Planetary Interiors*, 180(1–2), 92–103. <https://doi.org/10.1016/j.pepi.2010.01.011>

- Manaman, N. S., Shomali, H., & Koyi, H. (2011). New constraints on upper-mantle S-velocity structure and crustal thickness of the Iranian plateau using partitioned waveform inversion. *Geophysical Journal International*, 184(1), 247–267. <https://doi.org/10.1111/j.1365-246X.2010.04822.x>
- Moghaddam, M. J., Karimpour, M. H., Shafaroudi, A. M., Santos, J. F., & Corfu, F. (2021). Middle Eocene magmatism in the Khur region (Lut block, eastern Iran): Implications for petrogenesis and tectonic setting. *International Geology Review*, 63(9), 1051–1066. <https://doi.org/10.1080/00206814.2019.1708815>
- Mooney, W. D. (2015). *Crust and lithospheric structure—global crustal structure*. Elsevier.
- Mousavi, S. M. (2017a). Mapping seismic moment and b-value within the continental-collision orogenic-belt region of the Iranian Plateau. *Journal of Geodynamics*, 103, 26–41. <https://doi.org/10.1016/j.jog.2016.12.001>
- Mousavi, S. M. (2017b). Spatial variation in the frequency-magnitude distribution of earthquakes under the tectonic framework in the Middle East. *Journal of Asian Earth Sciences*, 147, 193–209. <https://doi.org/10.1016/j.jseas.2017.07.040>
- Nissen, E., Ghods, A., Karasözen, E., Elliott, J. R., Barnhart, W. D., Bergman, E. A., et al. (2019). The 12 November 2017 Mw 7.3 Ezgeleh-Sarpolzahab (Iran) earthquake and active tectonics of the Lurestan arc. *Journal of Geophysical Research: Solid Earth*, 124(2), 2124–2152. <https://doi.org/10.1029/2018jb016221>
- Nissen, E., Tatar, M., Jackson, J. A., & Allen, M. B. (2011). New views on earthquake faulting in the Zagros fold-and-thrust belt of Iran. *Geophysical Journal International*, 186(3), 928–944. <https://doi.org/10.1111/j.1365-246X.2011.05119.x>
- Omrani, J., Agard, P., Whitechurch, H., Benoit, M., Prouteau, G., & Jolivet, L. (2008). Arc-Magmatism and subduction history beneath the Zagros mountains, Iran: A new report of adakites and geodynamic consequences. *Lithos*, 106(3–4), 380–398. <https://doi.org/10.1016/j.lithos.2008.09.008>
- Ottmüller, L., Shapiro, N. M., Krishna Singh, S., & Pacheco, J. F. (2002). Lateral variation of Lg wave propagation in southern Mexico. *Journal of Geophysical Research*, 107(B1), ESE3-1–ESE3-13. <https://doi.org/10.1029/2001jb000206>
- Paige, C. C., & Saunders, M. A. (1982). LSQR: An algorithm for sparse linear equations and sparse least squares. *ACM Transactions on Mathematical Software*, 8(1), 43–71. <https://doi.org/10.1145/355984.355989>
- Pang, K.-N., Chung, S.-L., Zarrinkoub, M. H., Khatib, M. M., Mohammadi, S. S., Chiu, H.-Y., et al. (2013). Eocene–Oligocene post-collisional magmatism in the Lut–Sistan region, eastern Iran: Magma genesis and tectonic implications. *Lithos*, 180–181, 234–251. <https://doi.org/10.1016/j.lithos.2013.05.009>
- Pasyanos, M. E., Matzel, E. M., Walter, W. R., & Rodgers, A. J. (2009). Broad-band Lg attenuation modelling in the Middle East. *Geophysical Journal International*, 177(3), 1166–1176. <https://doi.org/10.1111/j.1365-246X.2009.04128.x>
- Pasyanos, M. E., Tarabulsi, Y. M., Al-Hadidy, S. Y., Raddadi, W. W., Mousa, A. D., El-Hussain, I., et al. (2021). Improved lithospheric attenuation structure of the Arabian Peninsula through the use of national network data. *Arabian Journal of Geosciences*, 14(10), 914. <https://doi.org/10.1007/s12517-021-07294-x>
- Pei, S., Sun, Y., & Toksöz, M. N. (2011). Tomographic Pn and Sn velocity beneath the continental collision zone from Alps to Himalaya. *Journal of Geophysical Research*, 116(B10), B10311. <https://doi.org/10.1029/2010jb007845>
- Rahmani, M., Motaghi, K., Ghods, A., Sobouti, F., Talebian, M., Ai, Y., & Chen, L. (2019). Deep velocity image of the north Zagros collision zone (Iran) from regional and teleseismic tomography. *Geophysical Journal International*, 219(3), 1729–1740. <https://doi.org/10.1093/gji/ggz393>
- Robert Engdahl, E., Jackson, J. A., Myers, S. C., Bergman, E. A., & Priestley, K. (2006). Relocation and assessment of seismicity in the Iran region. *Geophysical Journal International*, 167(2), 761–778. <https://doi.org/10.1111/j.1365-246X.2006.03127.x>
- Saccani, E., Delavari, M., Beccaluva, L., & Amini, S. (2010). Petrological and geochemical constraints on the origin of the Nehbandan ophiolitic complex (eastern Iran): Implication for the evolution of the Sistan Ocean. *Lithos*, 117(1–4), 209–228. <https://doi.org/10.1016/j.lithos.2010.02.016>
- Sadeghi-Bagherabadi, A., Sobouti, F., Ghods, A., Motaghi, K., Talebian, M., Chen, L., et al. (2018). Upper mantle anisotropy and deformation beneath the major thrust-and-fold belts of Zagros and Alborz and the Iranian Plateau. *Geophysical Journal International*, 214(3), 1913–1918. <https://doi.org/10.1093/gji/ggy233>
- Sereno, T. J., Bratt, S. R., & Bache, T. C. (1988). Simultaneous inversion of regional wave spectra for attenuation and seismic moment in Scandinavia. *Journal of Geophysical Research*, 93(B3), 2019–2035. <https://doi.org/10.1029/JB093iB03p02019>
- Sereno, T. J., & Given, J. W. (1990). Pn attenuation for a spherically symmetric Earth model. *Geophysical Research Letters*, 17(8), 1141–1144. <https://doi.org/10.1029/GL017i008p01141>
- Shahabpour, J. (2007). Island-arc affinity of the central Iranian volcanic belt. *Journal of Asian Earth Sciences*, 30(5–6), 652–665. <https://doi.org/10.1016/j.jseas.2007.02.004>
- Shomali, Z. H., Keshvari, F., Hassanzadeh, J., & Mirzaei, N. (2011). Lithospheric structure beneath the Zagros collision zone resolved by non-linear teleseismic tomography. *Geophysical Journal International*, 187(1), 394–406. <https://doi.org/10.1111/j.1365-246X.2011.05150.x>
- Stern, R. J., Moghadam, H. S., Pirouz, M., & Mooney, W. (2021). The geodynamic evolution of Iran. *Annual Review of Earth and Planetary Sciences*, 49(1), 9–36. <https://doi.org/10.1146/annurev-earth-071620-052109>
- Su, B.-X., Chung, S.-L., Zarrinkoub, M. H., Pang, K.-N., Chen, L., Ji, W.-Q., et al. (2014). Composition and structure of the lithospheric mantle beneath NE Iran: Constraints from mantle xenoliths. *Lithos*, 202–203, 267–282. <https://doi.org/10.1016/j.lithos.2014.06.002>
- Taghizadeh-Farahmand, F., Afsari, N., & Sodoudi, F. (2015). Crustal thickness of Iran inferred from converted waves. *Pure and Applied Geophysics*, 172(2), 309–331. <https://doi.org/10.1007/s00024-014-0901-0>
- van Hunen, J., & Allen, M. B. (2011). Continental collision and slab break-off: A comparison of 3-D numerical models with observations. *Earth and Planetary Science Letters*, 302(1–2), 27–37. <https://doi.org/10.1016/j.epsl.2010.11.035>
- Veisi, M., Sobouti, F., Chevrot, S., Abbasi, M., & Shabaniyan, E. (2021). Upper mantle structure under the Zagros collision zone; insights from 3D teleseismic P-wave tomography. *Tectonophysics*, 819, 229106. <https://doi.org/10.1016/j.tecto.2021.229106>
- Verdel, C., Wernicke, B. P., Hassanzadeh, J., & Guest, B. (2011). A Paleogene extensional arc flare-up in Iran. *Tectonics*, 30(3), TC3008. <https://doi.org/10.1029/2010tc002809>
- Walker, R. T., Gans, P., Allen, M. B., Jackson, J., Khatib, M., Marsh, N., & Zarrinkoub, M. (2009). Late Cenozoic volcanism and rates of active faulting in eastern Iran. *Geophysical Journal International*, 177(2), 783–805. <https://doi.org/10.1111/j.1365-246X.2008.04024.x>
- Wang, X., Chen, L., Talebian, M., Ai, Y., Jiang, M., Yao, H., et al. (2022). Shallow crustal response to Arabia-Eurasia convergence in northwestern Iran: Constraints from multifrequency P-wave receiver functions. *Journal of Geophysical Research: Solid Earth*, 127(9), e2022JB024515. <https://doi.org/10.1029/2022jb024515>
- Wortel, M. J. R., & Spakman, W. (2000). Subduction and slab detachment in the Mediterranean-Carpathian region. *Science*, 290(5498), 1910–1917. <https://doi.org/10.1126/science.290.5498.1910>

- Wu, Z., Chen, L., Talebian, M., Wang, X., Jiang, M., Ai, Y., et al. (2021). Lateral structural variation of the lithosphere-asthenosphere system in the northeastern to eastern Iranian Plateau and its tectonic implications. *Journal of Geophysical Research: Solid Earth*, *126*(1), e2020JB020256. <https://doi.org/10.1029/2020jb020256>
- Xie, J. K., & Patton, H. J. (1999). Regional phase excitation and propagation in the Lop Nor region of central Asia and implications for P/Lg discriminants. *Journal of Geophysical Research*, *104*(B1), 941–954. <https://doi.org/10.1029/1998jb900045>
- Xie, X. B., & Lay, T. (2017). Effects of laterally varying mantle lid velocity gradient and crustal thickness on Pn geometric spreading with application to the North Korean test site. *Bulletin of the Seismological Society of America*, *107*(1), 22–33. <https://doi.org/10.1785/0120160203>
- Yang, G., Chen, L., Zhao, L. F., Xie, X. B., & Yao, Z. X. (2023). Crustal Lg attenuation beneath the Iranian Plateau: Implications for Cenozoic magmatism related to slab subduction, slab break-off, and mantle flow. *Journal of Geophysical Research: Solid Earth*, *128*(3), e2022JB025664. <https://doi.org/10.1029/2022JB025664>
- Yang, G., Zhao, L. F., Xie, X. B., He, X., Lü, Y., & Yao, Z. X. (2022). “Double Door” opening of the Japan Sea inferred by Pn attenuation tomography. *Geophysical Research Letters*, *49*(16), e2022GL099886. <https://doi.org/10.1029/2022gl099886>
- Yang, H., Zhang, H., Xiao, W., Tao, L., Gao, Z., Luo, B., & Zhang, L. (2021). Multiple Early Paleozoic granitoids from the southeastern Qilian Orogen, NW China: Magma responses to slab roll-back and break-off. *Lithos*, *380–381*, 380–381. <https://doi.org/10.1016/j.lithos.2020.105910>
- Yang, X., Lay, T., Xie, X. B., & Thorne, M. S. (2007). Geometric spreading of Pn and Sn in a spherical Earth model. *Bulletin of the Seismological Society of America*, *97*(6), 2053–2065. <https://doi.org/10.1785/0120070031>
- Yang, X. N. (2011). A Pn spreading model constrained with observed amplitudes in Asia. *Bulletin of the Seismological Society of America*, *101*(5), 2201–2211. <https://doi.org/10.1785/0120100314>
- Zhao, L. F., Xie, X. B., Tian, B. F., Chen, Q. F., Hao, T. Y., & Yao, Z. X. (2015). Pn wave geometrical spreading and attenuation in Northeast China and the Korean Peninsula constrained by observations from North Korean nuclear explosions. *Journal of Geophysical Research: Solid Earth*, *120*(11), 7558–7571. <https://doi.org/10.1002/2015jb012205>
- Zhu, H., Bozdağ, E., Duffy, T. S., & Tromp, J. (2013). Seismic attenuation beneath Europe and the north Atlantic: Implications for water in the mantle. *Earth and Planetary Science Letters*, *381*, 1–11. <https://doi.org/10.1016/j.epsl.2013.08.030>